RSC Publishing Faraday Discussions

Photoelectron spectra of $Al_2O_2^-$ and $Al_3O_3^-$ via slow electron velocity-map imaging

Journal:	*Faraday Discussions*
Manuscript ID	FD-ART-11-2018-000165
Article Type:	Paper
Date Submitted by the Author:	05-Nov-2018
Complete List of Authors:	DeVine, Jessalyn; University of California, Dept. of Chemistry Babin, Mark; University of California, Dept of Chemistry Neumark, Daniel; University of California, Dept of Chemistry

Photoelectron spectra of $Al_2O_2^-$ and $Al_3O_3^-$ via slow electron velocity-map imaging

Jessalyn A. DeVine, Mark C. Babin, Daniel M. Neumark*

Department of Chemistry, University of California, Berkeley, California 94720, United States and Chemical Sciences Division, Lawrence Berkeley National Laboratory, Berkeley, California 94720, United States.

*Correspondence to: dneumark@berkeley.edu

Abstract

High-resolution photoelectron spectra of cryogenically-cooled $Al_2O_2^-$ and $Al_3O_3^-$ cluster anions are obtained using slow electron velocity-map imaging. These spectra show vibrationally-resolved detachment from the $\tilde{X}\ ^2B_{3u}$ ground state of $Al_2O_2^-$ to the $\tilde{X}\ ^1A_g$ and $\tilde{a}\ ^3B_{3u}$ neutral electronic states, giving an electron affinity of 1.87904(4) eV for neutral Al_2O_2 and a term energy of 0.4938(4) eV for the triplet excited state. Additionally, there is evidence for autodetachment from photoexcited anions as well as influences from vibronic coupling between excited states of the neutral Al_2O_2 cluster. Detachment from both the "kite" and "book" isomers of $Al_3O_3^-$ is observed, yielding electron affinities of 2.0626(4) and 2.792(3) eV for the corresponding neutral isomers. Experiments carried out at different anion temperatures suggest that the two anionic isomers are nearly isoenergetic but clearly identify the kite isomer as the global minimum structure, in contrast to prior studies. This finding is supported by density functional theory calculations, which show that the relative ordering of the anion isomers is sensitive to basis set size; calculations for the anion isomers at the B3LYP/aug-cc-pVQZ level find the kite isomer to lie 0.011 eV below the book isomer.

1. Introduction

Aluminum oxides are seen in a wide range of chemical environments and play important roles as ceramics,[1] components of atmospheric aerosols,[2] and catalytic supports.[3] Aluminum oxide nanoparticles have also been identified in dust particles surrounding brown dwarfs[4] and in supernova remnants.[5] Given the prevalence of these species in both bulk and nanoscale materials, there is considerable interest in understanding how their molecular properties scale with system size. This can be accomplished by investigating the spectroscopy and reactivity of size-selected aluminum oxide clusters.

Gas-phase metal oxide clusters involving a range of metallic centers have attracted much interest as model systems for reactive sites on bulk surfaces, and provide an avenue for understanding the development of chemical properties and behavior with cluster size and stoichiometry.[6-8] In the case of aluminum oxides, oxygen-deficient systems (Al_xO_y with $y < 3x/2$) are of particular interest, as these serve as models for oxygen vacancies on bulk Al_xO_y surfaces that are susceptible to water adsorption.[9] In this work, we use high-resolution anion photoelectron spectroscopy to probe the anionic and neutral charge states of two oxygen-deficient aluminum oxide clusters, Al_2O_2 and Al_3O_3, providing a substantial improvement in resolution over prior work and revealing new energetic and spectroscopic subtleties of these systems.

Some of the smaller neutral aluminum oxides have been isolated in N_2 and Ar matrices, yielding vibrational frequencies and structural characterization of Al_xO_y (x, y = 1-2).[10-13] Neutral clusters over a wider size range have been characterized using infrared resonance-enhanced multiphoton ionization, the results of which suggest that clusters converge to a γ-Al_2O_3-like geometry over the $AlO\cdot(Al_2O_3)_{0-34}$ series.[14, 15] Due to the important role that oxidation states play in the chemistry of aluminum oxides, ionic clusters are also of considerable interest, and infrared photodissociation experiments have yielded structural determination for both anionic and cationic Al_xO_y clusters.[16-19] Anion photoelectron spectroscopy (PES) is another structurally-sensitive spectroscopic technique which, in contrast to infrared experiments, informs on both the anionic and neutral states of a given molecule, and has been used to characterize the structural and electronic properties of several aluminum oxide clusters.[20-22] These experiments combined with

theoretical work[23] indicate that the most stable geometries of anionic and neutral Al_xO_y typically contain 3- or 4-membered rings, with the cyclic Al-O-Al-O substructure being particularly prevalent.

The smallest cluster for which this cyclic moiety is present is Al_2O_2, which was suggested to contribute to the infrared spectrum of the products formed from reaction of Al atoms with oxygen in argon matrices.[11] The anion photoelectron spectrum of $Al_2O_2^-$ reported by Desai *et al*.[20] provided a more definitive observation of this cluster. This spectrum was consistent with detachment from the rhombic structure **2a** shown in Fig. 1 and showed partial vibrational resolution for detachment to the $\tilde{X}\ ^1A_g$ and $\tilde{a}\ ^3B_{3u}$ neutral electronic states, giving vibrational frequencies of 660(80) and 730(80) cm^{-1} for the ground and excited neutral states, respectively. However, the authors noted that neither of these frequencies were consistent with the calculated values of totally symmetric modes and suggested that these instead correspond to averages of the frequencies of both a_g-symmetric modes in each state that could not be cleanly resolved.

The next-smallest cluster of the same stoichiometry, $Al_3O_3^-$, has received much attention since its photoelectron spectrum was first reported by Wu *et al*. in 1998.[21] These results showed two partially-resolved bands, *X'* and *X*, with band *X'* covering electron binding energies (eBEs) of ~2.0 – 2.5 eV and band *X* spanning eBEs of ~2.5 – 3.0 eV. These two regions of structure were attributed to detachment from two distinct anion isomers, though structural assignments were not made in this initial work. Subsequent experimental[22] and theoretical studies[24-26] identified these isomers as the kite (**3a**) and book (**3b**) isomers pictured in Fig. 1, with bands *X'* and *X* assigned to detachment from anion isomers **3a** and **3b**, respectively. These structures can be understood as forming from the **2a** geometry by end-on (**3a**) or side-on (**3b**) addition of an AlO unit to the Al_2O_2 ring, resulting in the formation of additional Al-O bonds. In the photoelectron spectrum of Wu and coworkers, the partially-resolved progressions in each band gave vibrational frequencies of 720(60) and 610(60) cm^{-1} for the kite and book neutral isomers, respectively. A somewhat higher resolution photoelectron spectrum was reported by Meloni *et al*,[22] who also saw detachment to an excited electronic state of isomer **3b**.

To determine which anion isomer contributing to the photoelectron spectrum corresponded to the lower-energy structure, Wu *et al.*[21] explored the effect of anion temperature on the relative intensities of each region of structure by varying the timing between the laser pulse and the carrier gas in their laser ablation ion source. In this analysis, a shorter time delay between ablation of the metal surface and injection of the carrier gas was assumed to result in the formation of warmer ions, as the ions in the plasma would have lower internal energies if allowed to collisionally cool for a longer duration before entrainment by the carrier gas. This study found that at shorter delays, the relative intensity of band *X´* was enhanced, leading to the inference that isomer **3b** corresponds to the anion global minimum of $Al_3O_3^-$. This energy ordering was supported by density functional theory (DFT) and configuration interaction (QCISD) calculations,[25, 26] though the calculated isomeric energies are typically small, with the kite anion isomer lying 30 and 200 meV higher in energy in the DFT and QCISD treatments, respectively.

Slow electron velocity-map imaging spectroscopy of cryogenically-cooled anions (cryo-SEVI) is a variant of anion PES wherein cold ions are detached with a tunable laser and the resultant electron kinetic energy distribution is analyzed by a velocity-map imaging (VMI) spectrometer that is optimized for the detection of slow electrons, yielding photoelectron spectra with sub-meV resolution.[27, 28] In the current work, the photoelectron spectra of $Al_2O_2^-$ and $Al_3O_3^-$ are revisited using cryo-SEVI, providing substantial improvements in resolution over previous work. In addition to well-resolved vibrational structure, the spectra of $Al_2O_2^-$ show evidence for autodetachment in the ground state singlet band and vibronic coupling between neutral excited states in the triplet band; these interpretations are supported by the measured photoelectron angular distributions across each band. Detachment from both isomers of $Al_3O_3^-$ is seen, despite the low ion temperatures associated with the cryo-SEVI experiment, reaffirming that the energy difference between anion isomers **3a** and **3b** is quite small. By explicitly varying the anion temperature and observing its effect on the photoelectron signals, we find the kite isomer **3a** to be the global minimum anion structure, in contrast to earlier work.[21, 22, 24-26] This conclusion is supported by new electronic structure calculations. Detachment from isomer **3a** is obtained in excellent resolution, yielding several vibrational

frequencies for totally-symmetric modes of the neutral doublet ground state. Due to unusual threshold behavior, detachment from anion isomer **3b** was not obtained in as high resolution, though the current results do show considerably more vibrational structure than has been resolved previously.

2. Experimental Methods

The cryo-SEVI method and apparatus have been described in detail previously. [29, 30] Aluminum oxide cluster anions are generated in a laser ablation ion source in which the frequency-doubled output of an Nd:YAG laser is focused onto a rotating and translating aluminum disk, generating a plasma. A pulse of helium carrier gas from an Even-Lavie valve[31] entrains the species present in the plasma, and this mixture passes through a narrow channel to facilitate collisional cooling and formation of clusters. The pulsed beam then expands into vacuum and the ions are directed through a radiofrequency (RF) hexapole ion guide and an RF quadrupole mass filter before being admitted into an RF octupole ion trap,[30] which is held at 5 K and filled with a buffer gas mixture of 20% H_2 in He. While confined in the trap, collisional energy transfer between the ions and the buffer gas cools the ions substantially, typically resulting in ions with temperatures on the order of 10 K.[32]

After ~40 ms of cooling, ions are extracted into an orthogonal Wiley-McLaren time-of-flight mass spectrometer[33] and focused into the interaction region of a VMI assembly.[34, 35] The ions of interest are photodetached by the output of a tunable dye laser pumped by either the second or third harmonic of an Nd:YAG laser. The resultant photoelectrons are projected onto a position-sensitive detector consisting of two chevron-stacked microchannel plates coupled to a phosphor screen, the back of which is photographed by a CCD camera.[36] Each photograph is analyzed for individual electron events whose centroids are tabulated.[37] The accumulated images are then circularized using the method described by Gascooke and coworkers[38] to correct for small angular distortions resulting from imperfect shielding in the field-free region. The maximum entropy velocity Legendre reconstruction (MEVELER) algorithm reconstructs the initial three-dimensional electron velocity distribution from the circularized images,[39] and the radii of

features in the reconstructed images are related to electron kinetic energy (eKE) by obtaining images for the well-known detachment transitions of atomic O^-, S^-, and F^- at several photon energies.[40-42]

In addition to the eKE distributions, VMI detection provides the photoelectron angular distribution (PAD) associated with each detachment transition, given by[43]

$$\frac{d\sigma}{d\Omega} = \frac{\sigma_{tot}}{4\pi}\left[1 + \beta P_2(\cos\theta)\right], \quad (1)$$

where σ_{tot} is the total detachment cross section, θ is the angle of the outgoing photoelectron's velocity vector with respect to the laser polarization axis, $P_2(x)$ is the second-order Legendre polynomial, and β is the anisotropy parameter. The anisotropy parameter ranges from -1 to +2 corresponding to detachment perpendicular or parallel to the laser polarization axis and is particularly useful in interpreting cryo-SEVI spectra as it reports on the electronic character of a detachment transition, allowing for distinction between transitions involving different electronic states.

Due to the approximately constant resolving power, ΔeKE/eKE, of the VMI detection method, the best resolution is obtained for low-eKE electrons. As such, a single cryo-SEVI spectrum is obtained first by acquiring an overview spectrum at a relatively high photon energy, and then by tuning the detachment energy to within several hundred cm^{-1} of each feature of interest to yield narrow high-resolution windows of the overall spectrum. These individual windows are then scaled to match relative intensities in the overview spectrum, where the relative peak intensities are not as strongly impacted by threshold behavior of the detachment cross section.[44] These data are displayed together to yield a full photoelectron spectrum with resolution as high as 1-2 cm^{-1}. As numerous photon energies are used to acquire a single SEVI spectrum, spectra are plotted as functions of eBE, given by eBE = $h\nu$ – eKE.

3. Computational Methods

To assign and interpret the cryo-SEVI spectra of $Al_2O_2^-$ and $Al_3O_3^-$, electronic structure calculations were performed using DFT as implemented in Gaussian 09.[45] For all systems, geometry optimizations and

frequency calculations were carried out at the B3LYP/aug-cc-pVTZ level, using tight convergence criteria and an ultrafine integration grid with 99 radial points and 590 angular points. In light of previous work concerning the structural assignment of the $Al_2O_2^-$ and $Al_3O_3^-$ anions,[22, 24-26, 46] only geometries **2a**, **3a**, and **3b** shown in Figure 1 were considered.

Calculations were performed for the lowest-energy doublet anion state ($\tilde{X}\ ^2B_{3u}$) of the $Al_2O_2^-$ anion as well as the lowest-energy singlet ($\tilde{X}\ ^1A_g$) and triplet ($\tilde{a}\ ^3B_{3u}$) states of the corresponding neutral; the resultant geometries and relative energies are provided in Table S1 of the Supporting Information (SI). For both isomers of Al_3O_3, the singlet anion and doublet neutral states were considered, and the resultant geometries and energies are provided in Table S2 of the SI. Calculated vibrational frequencies for both isomers of $Al_3O_3^{-/0}$ are provided in Table S3 of the SI, and those of $Al_2O_2^{-/0}$ will be considered below. In addition, a time-dependent DFT (TDDFT) calculation was carried out to find excitations of the triplet state of Al_2O_2, the results of which are provided in Table S4 of the SI.

The optimized geometries, normal modes, and harmonic frequencies obtained at the B3LYP/aug-cc-pVTZ level were used as input for the ezSpectrum software package[47] to calculate FC profiles for the $\tilde{X}\ ^1A_g \leftarrow \tilde{X}\ ^2B_{3u}$ and $\tilde{a}\ ^3B_{3u} \leftarrow \tilde{X}\ ^2B_{3u}$ detachment transitions of $Al_2O_2^-$ and the $\tilde{X}\ ^2A_1 \leftarrow \tilde{X}\ ^1A_1$ and $\tilde{X}\ ^2B_2 \leftarrow \tilde{X}\ ^1A_1$ detachment transitions of $Al_3O_3^-$ isomers **3a** and **3b**, respectively. All vibrational modes were treated as harmonic oscillators and Duschinsky mixing was used to account for differences between anion and neutral normal modes. To optimize the fit to experiment, the presented FC profiles for detachment from both isomers of $Al_3O_3^-$ use experimental frequencies for the FC-active modes of neutral isomers **3a** and **3b**.

Photodetachment cross sections and angular distributions based on the DFT anion molecular orbitals were calculated using the code of Liu and Ning.[48] This code models the outgoing electron (with momentum k) resulting from detachment from a specified anion orbital as a superposition of spherical waves with angular momenta $l < 6$. The expansion coefficients, C_{klm}, describe the amplitude of each

spherical wave component; from these, a fractional partial wave character, f_l, may be defined for a particular eKE as[49]

$$f_l = \frac{P_l}{\sum_{l=0}^{5} P_l} \quad \text{where} \quad P_l = \sum_{m=-l}^{l} C_{klm}^2 . \tag{2}$$

4. Experimental Results

1. Al_2O_2

The cryo-SEVI spectrum of $Al_2O_2^-$ is presented in Figure 2, covering the same two regions of structure observed previously.[20] Figure 2a shows the lower-eBE region of structure spanning eBEs of ~14500 to 17500 cm^{-1} and corresponding to the $\tilde{X}\ ^1A_g \leftarrow \tilde{X}\ ^2B_{3u}$ ground state band. The molecular orbital (MO) diagram of the $Al_2O_2^-$ anion obtained from DFT calculations is provided in Figure 3; the $\tilde{X}\ ^1A_g \leftarrow \tilde{X}\ ^2B_{3u}$ detachment transition corresponds to removal of an electron from the singly-occupied $5b_{3u}$ orbital. The higher-energy region of structure, shown in Figure 2b, spans eBEs from 18500 to 21000 cm^{-1} and coincides with the previously reported $\tilde{a}\ ^3B_{3u} \leftarrow \tilde{X}\ ^2B_{3u}$ excited state band. This electronic transition corresponds to removal of an electron from the doubly-occupied $7a_g$ orbital in Fig. 3.

The singlet band (Fig. 2a) shows four well-defined features (X1-X4) that are observed over the entire range of photon energies used to produce the composite spectrum in Fig. 2a, and these are ascribed (as is typically the case in photoelectron spectra) to direct detachment transitions terminating in various vibrational levels of the $\tilde{X}\ ^1A_g$ neutral state,

$$Al_2O_2^- + h\nu \rightarrow Al_2O_2 + e^- . \tag{3}$$

The binding energies of features X1-X4 are provided in Table 1. Peak X1 is assigned to the vibrational origin (the 0_0^0 photodetachment transition), giving an electron affinity of EA=1.8709(4) eV for the Al_2O_2 neutral cluster. For peaks X1-X3, sufficient intensity is maintained near-threshold to allow for low-eKE

scans, resulting peaks with ~7 cm^{-1} full-width at half-maximum (fwhm). Owing to the lower intensity of X4, its narrowest measurable peak width was 24 cm^{-1} fwhm. Features X1-X4 all show similar PADs (Fig. 4), with $\beta < 0$ over the range of photon energies used to construct Fig. 2a.

Peaks a-d in Fig. 2a exhibit notably different characteristics than peaks X1-X4. Figure 4 shows that the PADs of peaks a-d are characterized by positive values of β. Moreover, the relative intensities of peaks a-d demonstrate a complex dependence on photon energy. Figure 5 shows spectra taken at three different photon energies, illustrating the non-monotonic dependence of the intensity of peak a as a function of photon energy relative to those of two adjacent direct detachment features. At the lowest (15960 cm^{-1}) and highest (18866 cm^{-1}) photon energies shown in this Figure, peak a is not observed. Between these energies, the intensity of peak a relative to X2 and X3 rises and falls (Figure S1 of the SI), reaching a maximum intensity at around $h\nu$ = 16695 cm^{-1}. As can be seen in Fig. S1, similar behavior is observed for peak b, and both a and b are found to reach maximum intensities for photon energies which correspond to eKEs of around 900 cm^{-1}. Peaks c and d are less intense; hence, their dependence is more difficult to parse given the data shown in Fig. S1. However, we group them with peaks a and b based on their PADs.

The observed photon dependence suggests that transitions a-d result from autodetachment,

$$Al_2O_2^- + h\nu \rightarrow Al_2O_2^{-*} \rightarrow Al_2O_2 + e^- , \quad (4)$$

where the incident photon induces a transition to an electronically excited state of the anion which can spontaneously eject an electron. This mechanism will be discussed in Section 5.1.

In the triplet band (Fig. 2b), the cryo-SEVI spectra again provide much clearer vibrational structure than was observed in prior work, showing a number of features (T1-T6) with typical peak widths of ~8 cm^{-1} fwhm. The electron binding energies of these features are provided in Table 1. The PADs of these features (Fig. 4b) show that with the exception of T3, all features exhibit positive anisotropies for the observed kinetic energies. All features (including T3) show straightforward dependences of their relative intensities on photon energy, and thus can be attributed to direct detachment transitions terminating in various

vibrational levels of the triplet state of neutral Al_2O_2 (Eq. 3). The relative positions of the vibrational origin peaks X1 and T1 give a term energy of 0.4938(4) eV for the $\tilde{a}\ ^3B_{3u}$ neutral state.

2. Al_3O_3

The full cryo-SEVI spectrum of $Al_3O_3^-$ is presented in Figure 6a, showing two regions of structure as in previous work.[21, 22] The lower-eBE region, spanning eBEs of 16000 to 21000 cm^{-1}, was obtained in high resolution and is shown in more detail in Figure 6b. This region was previously attributed to detachment from anion isomer **3a**. In this region, a number of vibronic transitions (A1-A16) are resolved, with typical peak widths of 8 cm^{-1} fwhm. This electronic band shows a dominant progression with ~760 cm^{-1} spacing (A1-A4-A9-A15), in good agreement with the progression observed previously.[21, 22] With the improvement in resolution afforded by cryo-SEVI, this progression is found to be modulated by several less intense patterns. All features show similar anisotropies, with $\beta > 0$ for all observed eKEs, and the PAD of feature A1 is provided in Figure S2a of the SI.

The higher-eBE region, spanning ~22000 to 26000 cm^{-1} of eBE and previously assigned as detachment from anion isomer **3b**, was not obtained in high resolution, due to low-eKE noise at higher photon energies as well as the threshold behavior of features in this region. Figure S3 of the SI shows three scans taken at different photon energies; as can be seen, feature B1 does not become appreciably narrower with decreasing eKE, maintaining a peak width of 30 cm^{-1} fwhm for eKEs of 600 cm^{-1} and 300 cm^{-1}. Additionally, the two lower photon energies used in Fig. S3 result in non-negligible noise at low eKEs which overlaps with direct detachment features; this noise can also be seen in the high-eBE portion of the green trace in Fig. 6a. Regardless, the overview spectrum shown in Fig. 6a represents a significant improvement in resolution over previous results, showing the minor progressions which modulate the dominant structure resolved in prior experiments (B1-B4-B6).[21, 22] As in the lower-eBE region, the sign of β was found to be the same across the entire higher-eBE electronic band. The PAD for feature B1 is

provided in Fig. S2a of the SI, showing perpendicular detachment ($\beta < 0$) for the photon energies used to construct Fig. S3. The peak positions of features B1-B6 and A1-A16 are summarized in Table 2.

To ascertain which of the two anion isomers corresponds to the global minimum of the anion, a temperature-dependence study was carried out on $Al_3O_3^-$. Ion temperature can be quantitatively controlled in the cryo-SEVI experiment by changing the temperature of the octupole trap; increasing the trap temperature gave the results shown in Figure 7 for detachment from $Al_3O_3^-$. In addition to increased peak widths leading to greater spectral congestion (as expected for detachment from rovibrationally hot ions), a clear enhancement of the higher-eBE region is observed as temperature is increased from 5 to 250 K. To quantify this enhancement, the integrated intensities for the two spectral regions were calculated, giving the fractional contribution to the total electron signal from each region of structure. This analysis shows that the higher-eBE region accounts for 31%, 44%, and 56% of the total electron signal in the T = 5, 175, and 250 K scans. This demonstrates that, in contrast to previous findings,[21] the isomer giving rise to transitions A1-A16 is the lowest-energy anion isomer. The structural assignment of the anions giving rise to each region of structure will be discussed in Section 5.2.

5. Discussion

1. Al_2O_2

Ground State Band. The calculated FC profile for the $\tilde{X}\ ^1A_g \leftarrow \tilde{X}\ ^2B_{3u}$ detachment transition of $Al_2O_2^-$, shown as red sticks in Figure 2a, provides excellent agreement for features X1-X4, yielding assignments for all four peaks attributed to direct detachment. These assignments are provided in Table 1. All of these transitions correspond to FC-allowed detachment transitions terminating in totally-symmetric (a_g) vibrational levels, yielding vibrational frequencies for both a_g-symmetric modes (Fig. S4 in the SI) of the $\tilde{X}\ ^1A_g$ singlet state. These values are provided and compared to calculated values in Table 3**.** Transitions a-d are absent from the FC simulations, supporting our prior assertion that these do not arise from FC-allowed direct detachment.

The photoelectron angular distributions are an indication of the angular momentum composition of the outgoing electron, which in turn reflects the orbital from which the detached electron originated.[50] The calculated PAD for removal of an electron from the $5b_{3u}$ anion MO (Fig. 3) is shown as a solid black line in Fig. 4a, and agrees qualitatively with the anisotropies of features X1-X4, showing perpendicular detachment ($\beta < 0$) over the relevant range of eKEs. However, these PADs differ substantially from the anisotropies of features a-d, which exhibit predominantly parallel detachment ($\beta > 0$). This further emphasizes that these transitions have different electronic character than X1-X4.

The photon dependence of the relative intensities of transitions a-d (Figures 5 and S1) are a hallmark of autodetachment, wherein the incident photon results in an excitation of the anion rather than a direct transition to the neutral + free electron continuum (Eq. 3). This initially excited anion state then detaches via a nonadiabatic transition as described in Eq. 4. The entire physical process leading to the observation of features a-d thus involves three states, denoted Ψ_1^α, Ψ_2^α, and Ψ_3^α, where Ψ_i^α represents the vibronic wavefunction of the initial anion (1), excited anion (2), or final neutral state (3) participating in autodetachment transition α (a, b, c, or d). Given the low temperatures of ions probed with cryo-SEVI,[32] Ψ_1^α is taken to correspond to the vibrational ground state (0^0) of the ground anion electronic state ($^2B_{3u}$) for all four transitions. In the following discussion, we will consider possible assignments for the Ψ_2^α and Ψ_3^α states involved in transitions a-d.

Transitions a, b, c, and d each lie ~660 cm^{-1} above a FC-allowed transition (X1, X2, X3, and X4, respectively), suggesting that the final states Ψ_3^α differ from the neutral levels involved in X1-X4 by a single quantum of excitation in a vibrational mode with a frequency of 660 cm^{-1}. As Al_2O_2 only possesses two totally-symmetric modes (Fig. S4), both of which participate in the FC-allowed transitions X1-X4, this third mode must be non-totally-symmetric within the D_{2h} point group. Given the calculated frequencies in Table 3 for the singlet state of Al_2O_2, the b_{1g}-symmetric ν_3 mode is the most likely candidate. If this is the case, then the neutral levels Ψ_3^α involved in transitions a, b, c, and d correspond to the 3^1, 2^13^1, 1^13^1, and

$1^1 2^1 3^1$ vibrational levels, respectively, of the $\tilde{X}\ ^1A_g$ neutral, giving a frequency of 663(5) cm^{-1} for ν_3 (Table 3).

The photon energy at which the lowest-energy autodetachment transition reaches its maximum intensity (Figure S1) suggests that the autodetaching anion state has an excitation energy of around 2.0 eV. According to the MRMP2 treatment of the $Al_2O_2^-$ anion carried out by Sarker and coworkers,[46] the three lowest-energy anion excited states lie in this region, suggesting that the ^2A_g (1.81 eV), $^2B_{2u}$ (2.08 eV), and $^2B_{1u}$ (2.10 eV) states are candidates for Ψ_2^α. The ^2A_g excitation, formed by excitation of an electron from the $7a_g$ orbital to the $5b_{3u}$ orbital in Fig. 3, is the only candidate for which symmetry permits a nonzero oscillator strength for photoexcitation of the $\tilde{X}\ ^2B_{3u}$ anion ground state, suggesting that this is the state from which autodetachment occurs. In this case, autodetachment to the closed-shell singlet would involve a two-electron transition, with one electron moving from the $5b_{3u}$ orbital to the $7a_g$ orbital resulting in ejection of the other $5b_{3u}$ electron. This sort of two-electron mechanism is indicative of electronically-driven autodetachment, where the coupling to the continuum state occurs via electron correlation terms in the Hamiltonian. Similar mechanisms can be used to understand autodetachment from a variety of other systems, such as the metastable $5d6s6d$ state of the Ba^- atomic anion[51] as well as autoionization of the $^{1,3}\Delta_u$ Rydberg states of N_2.[52] In both of these cases, the ejection of an electron occurs simultaneously with relaxation of an electron in a higher-lying orbital, and the loss in internal electronic energy is converted into the kinetic energy of the outgoing electron.

Excited State Band. Good agreement between the reported FC simulations and experiment is also found for the $\tilde{a}\ ^3B_{3u} \leftarrow \tilde{X}\ ^2B_{3u}$ electronic band of $Al_2O_2^-$ shown in Fig. 2b, providing assignment of all features – with the exception of T3 – to FC-allowed transitions. Again, frequencies for both a_g-symmetric vibrational modes are extracted, and are provided in Table 3 alongside the B3LYP/aug-cc-pVTZ results. The PADs of these features are in good agreement with the calculated results for detachment from the $7a_g$ orbital in Fig. 3, as shown by the solid black line in Fig. 4b.

Transition T3 is notably absent from the FC simulation for the triplet band of the $Al_2O_2^-$ cryo-SEVI spectrum. This transition lies only ~40 cm^{-1} below the ν_1 fundamental (T4), suggesting that it involves excitation of either ν_5 or ν_6 (Fig. S4 in the SI) which have calculated frequencies lying ~50 cm^{-1} below that of ν_1 at the B3LYP/aug-cc-pVTZ level of theory (see Table 3). As their calculated values are within several cm^{-1} of each other (722 and 720 cm^{-1} for ν_5 and ν_6, respectively), further consideration is needed to definitively determine which mode participates in the cryo-SEVI spectrum. These modes have symmetries of b_{2u} and b_{3u}, respectively, and thus their involvement in the photoelectron spectrum can only occur through vibronic coupling with a Franck-Condon allowed vibrational level (such as the vibrational ground state) within another electronic state.

For vibronic coupling to occur between two states *a* and *b*, the direct product of their overall vibronic symmetries, $(\Gamma^a_{elec} \otimes \Gamma^a_{vib}) \otimes (\Gamma^b_{elec} \otimes \Gamma^b_{vib})$ where Γ^x_{elec} and Γ^x_{vib} are the electronic and vibrational symmetries of state *x*, must contain the totally symmetric representation within the relevant molecular point group.[53] In the current case, this gives two possibilities for electronic symmetries of the state coupled to the $\tilde{a}\ ^3B_{3u}$ triplet which could give rise to T3 in the spectrum. If T3 corresponds to the 5_0^1 transition, then this excited state must have B_{1g} symmetry, whereas the 6_0^1 transition would require coupling to an A_g-symmetric state. The MRMP2 calculations carried out by Sarker and coworkers[46] found that the lowest-lying triplet A_g and B_{1g} states lie 6.75 and 3.23 eV, respectively, above the $\tilde{a}\ ^3B_{3u}$ triplet. Given that the extent of vibronic coupling decreases with increasing energy separation, we assign peak T3 as the 5_0^1 transition, which appears through Herzberg-Teller coupling to the excited $^3B_{1g}$ state.

The observation of FC-forbidden levels through Herzberg-Teller coupling has been seen in a number of cryo-SEVI spectra, where the PAD is often a key indicator of vibronic coupling.[54-57] The assignment of T3 as arising through this coupling mechanism suggests that the electronic character of this transition – reflected in its PAD – should match that expected for detachment to the excited $^3B_{1g}$ neutral state. A TDDFT calculation was performed at the B3LYP/aug-cc-pVTZ level to identify the orbital

transition giving rise to the lowest-energy state of this symmetry (Table S4 of the SI), finding that this $^3B_{1g}$ state can be formed from the anion ground state by removal of an electron from the $4b_{2u}$ orbital shown in Figure 3. The calculated PAD for detachment from this orbital yields the solid blue line shown in Fig. 4b, demonstrating perpendicular detachment over the relevant eKE range. This agrees with the observed PAD for feature T3, confirming our assignment of this transition as arising from vibronic coupling to the $^3B_{1g}$ state.

2. Al_3O_3

Lower-eBE Region. The lower-eBE region of the $Al_3O_3^-$ photoelectron spectrum was obtained in high resolution, as shown in Fig. 6b. This region of structure was previously attributed to detachment from anion isomer **3a**, and a FC simulation for detachment from this structure (shown as red sticks in Fig. 6b) indeed provides good agreement with the experimental spectrum. Additionally, the position of feature A1 gives an EA of 2.0626(5) eV, in excellent agreement with the B3LYP/aug-cc-pVTZ value of 2.078 eV for neutral isomer **3a**. Thus, as in prior works, this region of the $Al_3O_3^-$ spectrum is attributed to detachment from the **3a** "kite" anion. This isomer can be understood as derived from the **2a** rhombic structure of $Al_2O_2^-$, where the added AlO unit connects end-on by the O to one of the ring Al atoms forming the "tail" of the kite.

The good agreement between the cryo-SEVI spectrum and the calculated FC profile for the kite anion isomer provides assignment of all resolved peaks (A1-A16) as FC-allowed detachment to totally-symmetric vibrational levels of the neutral. The dominant structure (A1-A4-A9-A15) is assigned as a progression along ν_3, which corresponds to a totally-symmetric (in C_{2v}) distortion of the rhombic substructure of the kite isomer (Fig. S5 in the SI). The shift of peak A4 relative to A1 gives a frequency of 765(5) cm^{-1} for this mode, which is consistent with the ~770 cm^{-1} progression observed previously.[21, 22] In addition to this dominant progression, several other, less intense patterns are resolved, enabling extraction of frequencies for ν_2, ν_4, and ν_5; these values are provided in Table 4 and compared to the B3LYP/aug-cc-pVTZ results.

The particularly high FC activity of the ν_3 mode may be understood by considering the highest-occupied molecular orbital (HOMO) for the kite anion. As can be seen in Figure 8, the anion HOMO for isomer **3a** is an orbital with a_1-symmety primarily localized on the ring Al atom that does not bond to the "tail" of the kite, and possesses some antibonding character resulting in longer Al-O bond lengths for that part of the anion geometry. These Al-O bond lengths decrease by 0.1 Å following detachment from the anion to the neutral ground state (1.86 and 1.76 Å for anionic and neutral **3a**, respectively), owing to the removal of an electron from this orbital.

The calculated PAD for detachment from this orbital was also found to be consistent with the observed anisotropies of features A1-A16 (Fig. S2a). A partial wave analysis of the PAD calculation (Table S5) demonstrates that at low eKEs, *s*-wave detachment dominates, resulting in near-isotropic detachment. At higher eKEs (~2 eV), *p*-wave detachment dominates, giving the parallel detachment ($\beta > 0$) observed experimentally for features A1-A16. The high-eKE partial wave analysis agrees with the expected PAD based on the *s*&*p* model,[50] which considers the molecular orbital as containing primarily *s* and *p* character resulting in various contributions of outgoing *s*, *p*, and *d*-wave electrons. For detachment from an a_1-symmetric molecular orbital at moderate eKEs, parallel detachment is expected, corresponding to positive β-parameters associated with predominantly *p*-wave detachment.

Higher-eBE Region. Due to low-eKE noise present for detachment with higher photon energies than those used in Fig. 6b and the threshold behavior demonstrated in Fig. S3, as well as increasing spectral congestion at higher binding energies, the higher-eBE region of structure of the $Al_3O_3^-$ photoelectron spectrum was not obtained in as high resolution as the lower-eBE region. Regardless, the overview spectrum in Fig. 6a (where the low-eKE noise does not overlap with the dominant vibrational structure) shows substantial improvement in resolution for this region of the spectrum, and provides excellent agreement with the FC profile for detachment from anion isomer **3b**. The first intense feature in this part of the spectrum (B1) gives an EA of 2.792(3) eV, which is in reasonable agreement with the B3LYP/aug-cc-pVTZ value of 2.589 eV for neutral isomer **3b**. Thus, we attribute peaks B1-B6 as arising from anion

isomer **3b**, as in prior work. This structure can be understood as the result of side-on addition of an AlO unit to the rhombic **2a** geometry of $Al_2O_2^-$, resulting in a bicyclic structure with two additional Al-O bonds.

The agreement between the calculated FC profile in Fig. 6a and the experimental spectrum provides vibrational assignment of peaks B1-B6 as FC-allowed transitions terminating in totally-symmetric vibrational levels of neutral isomer **3b**. The dominant progression resolved in prior work,[21, 22] B1-B4-B6, is assigned as a progression along the ν_2 mode (Fig. S5), which corresponds to the stretching motion of the Al-O bonds forming the "page" edges of the book geometry. The B1-B4 peak spacing gives a frequency of 760(70) cm^{-1} for this mode; while this is closer to the calculated value of the ν_1 frequency for this neutral state, ν_1 was found to have very little FC activity in the simulations of Fig. 6a. The ν_4 and ν_5 fundamentals are also observed, giving the frequencies provided in Table 4.

As was the case for the lower-eBE region of structure, the dominant progression in the detachment spectrum of isomer **3b** can be understood by considering the anion HOMO from which an electron is removed to form the doublet neutral (Fig. 8). While slightly more delocalized than the HOMO for anion isomer **3a**, the corner Al atoms on the "pages" of the book possess significantly more electron density than the other atoms, and again there is some Al-O antibonding character. Removal of an electron from this b_2-symmetric orbital results in a decrease in the Al-O bond length on the outer edge of the "pages", from 1.87 Å in the anion to 1.80 Å in the neutral. This geometry change results in particularly high FC activity of the ν_2 mode pictured in Fig. S5.

The experimental PADs of features B1-B6 are consistent with this structural assignment (Fig. S2a). The partial wave analysis in Table S5 shows that at low eKEs, *s*-wave detachment dominates, and the *d*-wave contribution increases as eKE increases. This is again consistent with the *s*&*p* model of photoelectron angular distributions,[50] which dictates that detachment from a b_2-symmetric orbital should primarily result in perpendicular detachment corresponding to outgoing electrons with even *l* to give negative β parameters. From the partial wave analysis for the two isomers, it would be expected that B1-B6 would be able to be observed in higher resolution than is ultimately achieved, as isomer **3b** should undergo predominantly *s*-

wave detachment at lower eKEs, with a larger f_0 at an eKE of 0.001 eV than the **3a** isomer (f_0 = 0.868 and 0.993 for **3a** and **3b**, respectively). However, while features B1-B6 do maintain intensity near-threshold, the features do not become appreciably narrower, with nearly identical peak widths of ~30 cm^{-1} fwhm at eKEs of ~600 and 300 cm^{-1} (Fig. S3). The cause of the limited attainable resolution for detachment from the book isomer is somewhat unclear given the current results, though some speculation is possible.

One possibility is that the book isomer may be able to isomerize to the lower-lying kite isomer, resulting in a short-lived neutral which couples to the dense manifold of **3a** vibrational states, resulting in broadening of the cryo-SEVI peaks. To consider this possibility, a transition state calculation was performed on the neutral doublet surface of Al_3O_3 to identify a saddle point which connects isomers **3a** and **3b**. From this, the HPC algorithm[58, 59] was used to calculate the intrinsic reaction path, giving the potential energy curve provided in Fig. S6. These calculations show that the saddle point for the book/kite isomerization of neutral Al_3O_3 lies much closer in geometry and energy to the book isomer, with the transition state lying 110 meV above isomer **3b.** This could potentially result in a relatively short-lived neutral isomer **3b** that is capable of isomerization to isomer **3a** following its formation by photodetachment from the corresponding $Al_3O_3^-$ anion isomer, leading to contributions from a range of neutral levels in the observed detachment transitions. It should be emphasized that this is a highly speculative argument; a full theoretical treatment aimed at determining the relationship between isomerization and the observed near-threshold behavior is beyond the scope of the current work.

$Al_3O_3^{-/0}$ Energetics. Previous theoretical work on the $Al_3O_3^-$ anionic cluster have suggested that both isomers, **3a** and **3b** in Fig. 1, contribute to the photoelectron spectrum and are quite close in energy.[22, 25, 26] In the work of Martinez and coworkers,[25] the book was found to lie 30 meV lower than the kite isomer at the B3LYP/6-311+G(2d) level, and the energy difference increased to 200 meV with a QCISD treatment. While these energies were not corrected for zero-point energies (ZPEs), the frequencies of both isomers published in a subsequent paper[26] show that accounting for ZPEs does not result in a different energetic ordering, though it does decrease the energy difference to 21 meV at the B3LYP/6-311+G(2d) level. The

energy ordering was found to switch for the neutral cluster, with the kite lying ~0.5 eV below the book. DFT calculations were also reported by Meloni and coworkers,[22] who again found that isomer **3b** was lower in energy, giving a ZPE-corrected energy of 51 meV for isomer **3a** at the B3LYP/cc-pVTZ level.

The assignment of isomer **3b** as the global anion minimum was consistent with the temperature-dependence of the photoelectron spectra determined by Wu *et al*,[21] whose results suggested that increasing the temperature increased the intensity of the region attributed to detachment from anion isomer **3a**. However, the spectra shown in Figure 7 directly contradict this finding, showing that increasing ion temperature results in an enhancement of signal in the higher-eBE region attributed to detachment from anion isomer **3b**. This disagreement stems from the method used to control ion temperature in the current experiments versus the analysis of Wu *et al*, who assumed a straightforward relationship between the timing of the laser pulse and the carrier gas in their laser ablation source. In cryo-SEVI, ion temperature can be controlled directly by adjusting the cryostat connected to the ion trap, changing the temperature to which trapped ions thermalize through collisions with the buffer gas. Thus, the results in Figure 7 can be taken to represent the true temperature-dependence of the $Al_3O_3^-$ photoelectron spectrum.

In the current work, the same functional used in previous DFT treatments (B3LYP) was used with the aug-cc-pVTZ basis set. The B3LYP/aug-cc-pVTZ method gives a different isomeric energy ordering, with isomer **3a** lying only 5 meV lower when accounting for zero-point effects. This result illustrates that this system, specifically the relative energies of the $Al_3O_3^-$ anion isomers, is highly sensitive to basis set choice. In particular, prior treatments used basis sets which do not include diffuse functions, which is a key component of successful quantum chemical calculations on molecular anions, where the excess charge can result in relatively diffuse molecular orbitals. To further explore the basis set dependence of the isomeric energies, additional geometry optimizations and frequency calculations were carried out using the B3LYP functional with the aug-cc-pVDZ and aug-cc-pVQZ basis sets, giving the zero-point corrected energies shown in Table 5. While the aug-cc-pVDZ results agree with prior work that anion isomer **3b** is lower in energy, isomer **3a** becomes increasingly stable with the use of larger basis sets. Thus, given the temperature

dependence observed in Figure 7, it is clear that anion isomer **3a** is, in fact, the global minimum structure for the $Al_3O_3^-$ cluster. It should be noted that the structural assignments based on FC profiles and electron affinities agree with prior results; the current assessment of the $Al_3O_3^-$ photoelectron spectrum only differs in the assignment of which isomer is more stable.

Given the small energy difference between anions **3a** and **3b** implied by the experiemntal observation of both isomers despite low ion temperatures, the difference between the electron affinities of neutral isomers **3a** and **3b** can be taken as largely arising due to the relative stability of neutral isomer **3a**, giving an upper bound of 0.729 eV for the energy of neutral isomer **3b** relative to **3a**. This is in fair agreement with the calculated value of 0.506 eV for this energy difference at the B3LYP/aug-cc-pVTZ level. Thus, the current work enables structural assignment of two charge states of Al_3O_3, with isomer **3a** being the lowest-energy structure for both anion and neutral. Further, the potential for isomerization explored in the previous section and Fig. S6 of the SI demonstrate that the neutral book isomer is quite close in geometry to the book/kite transition state, which may result in relatively facile isomerization following photodetachment to form neutral isomer **3b**.

6. Conclusions

High-resolution anion photoelectron spectra of two aluminum suboxide clusters, $Al_2O_2^-$ and $Al_3O_3^-$, are obtained using slow electron velocity-map imaging of cryogenically-cooled anions. In both cases, the resultant spectra show improved resolution over prior results, and the observed vibrational structure is consistent with FC simulations based on B3LYP/aug-cc-pVTZ calculations, yielding a number of vibrational frequencies for neutral Al_2O_2 and Al_3O_3.

The $Al_2O_2^-$ anion is assigned, as in prior studies, to the D_{2h} rhombic geometry, which has been identified as a structural motif in larger aluminum oxide clusters. Detachment to two states of neutral Al_2O_2 is observed in high resolution. The ground state band, which corresponds to detachment to form a closed-shell singlet, shows several transitions that are attributed to autodetachment, and tentative assignments of

the anion excitation and final neutral states are provided. The triplet band of the cryo-SEVI spectrum shows evidence for Herzberg-Teller coupling between excited triplet states of the neutral cluster resulting in the appearance of nominally FC-forbidden levels.

As in previously reported photoelectron spectra, the cryo-SEVI spectra of $Al_3O_3^-$ show evidence of two coexisting anion isomers, identified as the kite and book geometries. While the observation of both isomers under the cold conditions of the cryo-SEVI experiment reaffirms the previously noted small energy difference between these two isomers, a controlled temperature study as well as B3LYP/aug-cc-pVTZ calculations establish the kite isomer as the global minimum of the anion. This is in contrast to previous experimental and theoretical work which found that the book isomer was lower in energy. The cause of the experimental discrepancy is attributed to the indirect method used to control ion temperature in previous experiments. The theoretical discrepancy likely arises due to the use of non-augmented basis sets in prior work, highlighting the importance of careful consideration of the theoretical treatments of gas phase metal oxide clusters, particularly in cases where multiple low-lying isomers are expected.

Conflicts of Interest

There are no conflicts of interest to declare.

Acknowledgments

JAD thanks Diptarka Hait for helpful conversations concerning the computational details of this work. This work is funded by the Air Force Office of Scientific Research under Grant No. FA9550-16-1-0097. MCB thanks the Department of Defense for a National Defense Science and Engineering graduate fellowship.

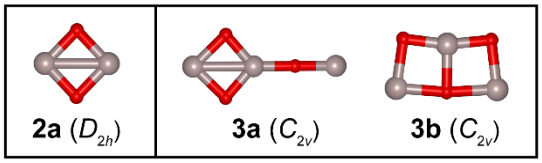

Figure 1. Isomers of (left) $Al_2O_2^{-/0}$ and (right) $Al_3O_3^{-/0}$ considered in the current work.

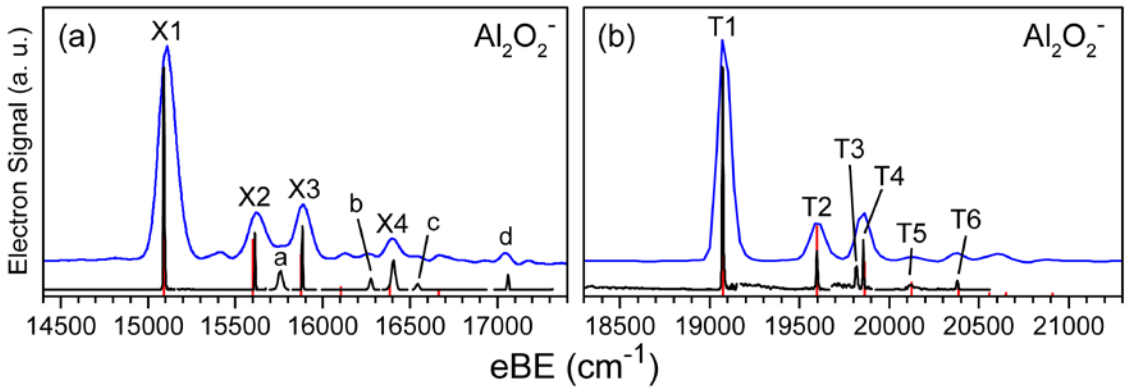

Figure 2. Cryo-SEVI spectra of $Al_2O_2^-$ showing detachment to the (a) singlet and (b) triplet states of neutral Al_2O_2. Blue traces are low-resolution overview scans taken with photon energies of 19154 and 23514 cm^{-1} in panels (a) and (b), respectively. Black traces are high-resolution scans taken at variable photon energies, and the red stick spectra show the results of the FC simulations for detachment from the **2a** anion.

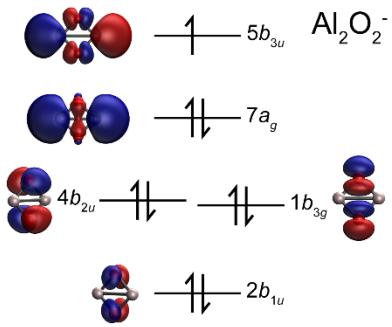

Figure 3. Molecular orbital diagram showing several of the highest-lying occupied orbitals of the $Al_2O_2^-$ anion as calculated at the B3LYP/aug-cc-pVTZ level.

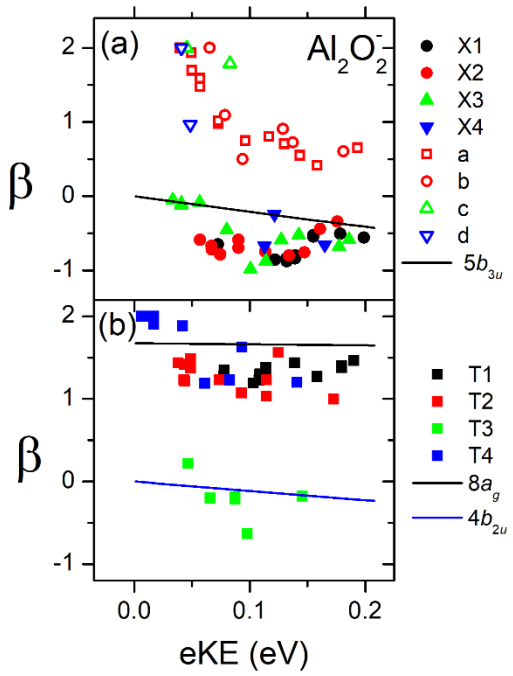

Figure 4. Anisotropy parameters for features observed in the (a) ground and (b) excited state bands of the $Al_2O_2^-$ cryo-SEVI spectrum. In both panels, the solid lines show the calculated anisotropy parameters for detachment from the indicated molecular orbitals of the $^2B_{3u}$ anion.

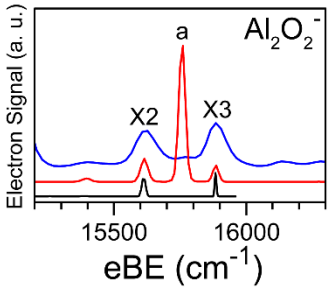

Figure 5. Cryo-SEVI scans taken at photon energies of 18866 cm^{-1} (blue), 16695 cm^{-1} (red), and 15960 cm^{-1} (black), illustrating the non-monotonic dependence of the relative intensity of peak a in the detachment spectrum of $Al_2O_2^-$. All traces have been normalized to the peak intensity of feature X1.

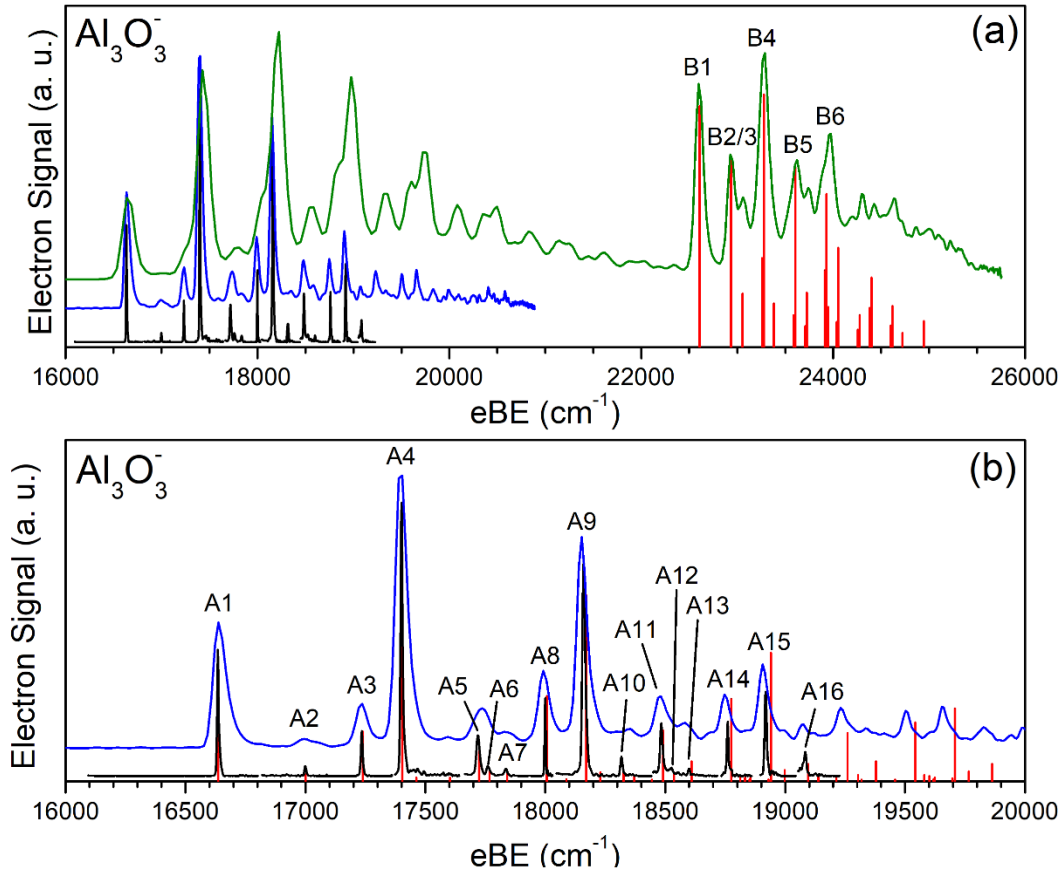

Figure 6. Cryo-SEVI spectra of $Al_3O_3^-$. (a) Full spectrum showing both regions of structure. The green and blue traces, taken with photon energies of 25757 and 20864 cm^{-1}, are lower-resolution overview scans for the higher-eBE and lower-eBE regions, respectively. The black traces are high-resolution scans taken with variable photon energies, and the red stick spectrum shows a Franck-Condon simulation for detachment from the **3b** anion isomer based on B3LYP/aug-cc-pVTZ results. (b) An expanded view of the lower-eBE region of structure, as well as a Franck-Condon simulation for detachment from the **3a** anion isomer shown as red sticks.

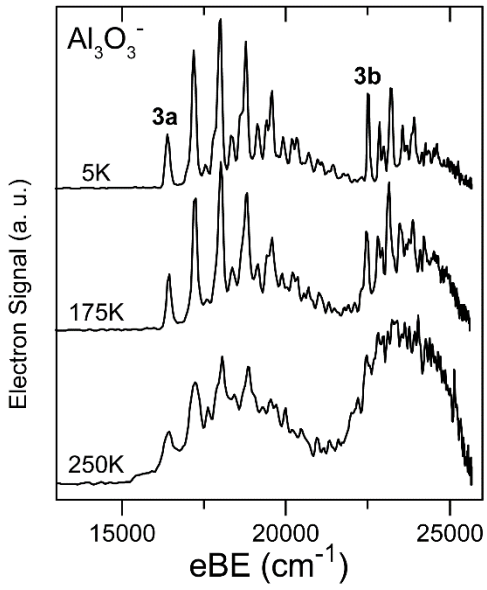

Figure 7. Detachment spectra of $Al_3O_3^-$ taken with a photon energy of 25663 cm^{-1} at a number of trap temperatures.

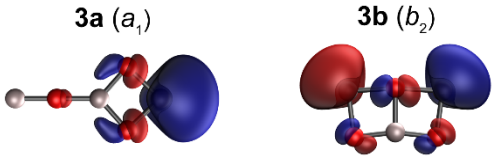

Figure 8. Highest-occupied molecular orbitals for the **3a** (left) and **3b** (right) isomers of the $Al_3O_3^-$ anion, as well as their symmetries within the C_{2v} point group.

Table 1. Peak positions (in cm^{-1}) for features observed in both electronic bands of the cryo-SEVI spectrum of $Al_2O_2^-$. For each feature, the shift from the appropriate vibrational origin (X1 or T1) is provided, in units of cm^{-1}. Assignments are provided for all transitions attributed to direct detachment. Uncertainties in peak positions correspond to one standard deviation from a gaussian fit to the highest-resolution experimental trace for each feature.

Peak	eBE	Shift	Assignment
	$\tilde{X}\ ^1A_g \leftarrow \tilde{X}\ ^2B_{3u}$		
X1	15090(3)	0	0_0^0
X2	15613(3)	523	2_0^1
a	15753(4)	663	
X3	15884(3)	794	1_0^1
b	16276(6)	1186	
X4	16405(11)	1315	$1_0^1 2_0^1$
c	16544(5)	1454	
d	17062(6)	1971	
	$\tilde{a}\ ^3B_{3u} \leftarrow \tilde{X}\ ^2B_{3u}$		
T1	19073(3)	0	0_0^0
T2	19599(3)	526	2_0^1
T3	19818(6)	745	5_0^1
T4	19856(3)	783	1_0^1
T5	20126(20)	1053	2_0^2
T6	20380(4)	1307	$1_0^1 2_0^1$

Table 2. Peak positions (in cm^{-1}) and vibrational assignments for features observed in the cryo-SEVI spectrum of $Al_3O_3^-$. For each feature, the shift from the appropriate vibrational origin (A1 or B1) is also provided in units of cm^{-1}, as is the sign of the anisotropy parameter β. The uncertainties in peak positions show the width parameter obtained from a Gaussian fit to the experimental peak.

Peak	eBE	Shift	Assignment	β
A1	16636(3)	0	0_0^0	+
A2	16999(3)	364	5_0^1	+
A3	17235(4)	599	4_0^1	+
A4	17401(4)	765	3_0^1	+
A5	17719(6)	1084	1_0^1	+
A6	17762(6)	1126	$3_0^1 5_0^1$	+
A7	17836(5)	1200	4_0^2	+
A8	18000(2)	1364	$3_0^1 4_0^1$	+
A9	18161(5)	1525	3_0^2	+
A10	18318(4)	1682	$1_0^1 4_0^1$	+
A11	18484(5)	1848	$1_0^1 3_0^1$	+
A12	18525(4)	1889	$3_0^2 5_0^1$	+
A13	18599(3)	1963	$3_0^1 4_0^2$	+
A14	18760(3)	2124	$3_0^2 4_0^1$	+
A15	18918(4)	2283	3_0^3	+
A16	19082(6)	2446	$1_0^1 3_0^1 4_0^1$	+
B1	22522(26)	0	0_0^0	-
B2	22867(27)	345	5_0^1	-
B3	22991(10)	470	4_0^1	-
B4	23278(59)	757	2_0^1	-
B5	23619(95)	1098	$2_0^1 5_0^1$	-
B6	23951(88)	1429	2_0^2	-

Table 3. Calculated and experimental values (in cm^{-1}) of the vibrational frequencies of anionic and neutral Al_2O_2, as well as their symmetries within the D_{2h} point group.

		$\tilde{X}\ ^2B_{3u}$	$\tilde{X}\ ^1A_g$		$\tilde{a}\ ^3B_{3u}$	
mode	sym.	theo.	theo.	exp.	theo.	exp.
ν_1	a_g	736	787	794(4)	770	783(4)
ν_2	a_g	476	504	523(4)	509	526(5)
ν_3	b_{1g}	566	617	663(5)*	608	
ν_4	b_{1u}	236	289		261	
ν_5	b_{2u}	683	751		722	745(7)
ν_6	b_{3u}	506	544		720	

*This value assumes that the autodetachment features a-d terminate in vibrational states with odd quanta of excitation along ν_3.

Table 4. Calculated and experimental values (in cm^{-1}) of the vibrational frequencies of both neutral isomers of Al_3O_3 probed in the current work. For both isomers, all extracted frequencies correspond to totally symmetric (a_1) modes within the C_{2v} point group.

	3a, $\tilde{X}\ ^2A_1$		**3b**, $\tilde{X}\ ^2B_2$	
mode	theo.	exp.	theo.	exp.
ν_1	1073	1084(7)	726	
ν_2	802		644	760(70)
ν_3	746	765(5)	573	
ν_4	586	599(5)	432	470(30)
ν_5	343	364(5)	246	350(40)

Table 5. Relative zero-point corrected energies of the $Al_3O_3^-$ isomers, in eV, calculated using the B3LYP functional with the indicated basis sets.

	aug-cc-pVDZ	**aug-cc-pVTZ**	**aug-cc-pVQZ**
3a	0.138	0.000	0.000
3b	0.000	0.005	0.011

References

1. P. Boch and T. Chartier, in *Ceramic Materials: Processes, Properties and Applications*, Wiley, Hoboken, 2010.
2. P. Warneck, in *Chemistry of the Natural Atmosphere*, Elsevier, Amsterdam, 2nd edn., 1999, vol. 71.
3. M. Trueba and S. P. Trasatti, *Eur. J. Inorg. Chem.*, 2005, **17**, 3393.
4. C. Helling and P. Woitke, *Astron. Astrophys.*, 2006, **455**, 325.
5. C. Biscaro and I. Cherchneff, *Astron. Astrophys.*, 2014, **564**, A25.
6. H.-J. Zhai and L.-S. Wang, *Chem. Phys. Lett.*, 2010, **500**, 185-195.
7. A. W. Castleman, *Catal. Lett.*, 2011, **141**, 1243-1253.
8. S. M. Lang and T. M. Bernhardt, *Phys. Chem. Chem. Phys.*, 2012, **14**, 9255-9269.
9. G. E. Brown., V. Henrich, W. Casey, D. Clark, C. Eggleston, A. Felmy, D. W. Goodman, M. Grätzel, G. Maciel, M. I. McCarthy, K. H. Nealson, D. A. Sverjensky, M. F. Toney and J. M. Zachara, *Chem. Rev.*, 1999, **99**, 77.
10. D. M. Makowiecki, J. Denis A. Lynch and K. D. Carlson, *J. Phys. Chem.*, 1971, **75**, 1963.
11. L. V. Serebrennikov, S. B. Osin and A. A. Maltsev, *J. Mol. Spec.*, 1982, **81**, 25.
12. S. M. Sonchik, L. Andrews and K. D. Carson, *J. Phys. Chem.*, 1983, **87**, 2004.
13. L. Andrews, T. R. Burkholder and J. T. Yustein, *J. Phys. Chem.*, 1992, **96**, 10182.
14. D. van Heijnsbergen, K. Demyk, M. A. Duncan, G. Meijer and G. von Helden, *Phys. Chem. Chem. Phys.*, 2003, **5**, 2515-2519.
15. K. Demyk, D. van Heijnsbergen, G. von Helden and G. Meijer, *Astron. Astrophys.*, 2004, **420**, 547-552.
16. M. Sierka, J. Dobler, J. Sauer, G. Santambrogio, M. Brummer, L. Woste, E. Janssens, G. Meijer and K. R. Asmis, *Angew. Chem. Int. Ed.*, 2007, **46**, 3372-3375.
17. G. Santambrogio, E. Janssens, S. Li, T. Siebert, G. Meijer, K. R. Asmis, J. Döbler, M. Sierka and J. Sauer, *J. Am. Chem. Soc.*, 2008, **130**, 15143.
18. X. Song, M. R. Fagiani, S. Gewinner, W. Schöllkopf, K. R. Asmis, F. A. Bischoff, F. Berger and J. Sauer, *J. Chem. Phys.*, 2016, **144**, 244305.
19. X. Song, M. R. Fagiani, S. Gewinner, W. Schöllkopf, K. R. Asmis, F. A. Bischoff, F. Berger and J. Sauer, *Chem. Phys. Chem.*, 2017, **18**, 868.
20. S. R. Desai, H. Wu and C. M. Rohlfing, *J. Chem. Phys.*, 1997, **106**, 1309.
21. H. Wu, X. Li, X.-B. Wang, C.-F. Ding and L.-S. Wang, *J. Chem. Phys.*, 1998, **109**, 449.
22. G. Meloni, M. J. Ferguson and D. M. Neumark, *Phys. Chem. Chem. Phys.*, 2003, **5**, 4073.
23. A. B. C. Patzer, C. Chang, E. Sedlmayr and D. Sülzle, *Eur Phys J D*, 2005, **32**, 329.
24. T. K. Ghanty and E. R. Davidson, *J Phys Chem A*, 1999, **103**, 8985.
25. A. Martínez, F. J. Tenorio and J. V. Ortiz, *J Phys Chem A*, 2001, **105**, 8787.
26. A. Martinez, L. E. Sansores, R. Salcedo, F. J. Tenorio and J. V. Ortiz, *J Phys Chem A*, 2002, **106**, 10630.
27. D. M. Neumark, *J Phys Chem A*, 2008, **112**, 13287-13301.
28. M. L. Weichman and D. M. Neumark, *Annu. Rev. Phys. Chem.*, 2018, **69**, 4.
29. A. Osterwalder, M. J. Nee, J. Zhou and D. M. Neumark, *J. Chem. Phys.*, 2004, **121**, 6317-6322.
30. C. Hock, J. B. Kim, M. L. Weichman, T. I. Yacovitch and D. M. Neumark, *J. Chem. Phys.*, 2012, **137**, 244201.
31. U. Even, J. Jortner, D. Noy, N. Lavie and C. Cossart-Magos, *J. Chem. Phys.*, 2000, **112**, 8068-8071.
32. J. B. Kim, C. Hock, T. I. Yacovitch and D. M. Neumark, *J Phys Chem A*, 2013, **117**, 8126-8131.
33. W. C. Wiley and I. H. Mclaren, *Rev. Sci. Instrum.*, 1955, **26**, 1150-1157.
34. A. T. J. B. Eppink and D. H. Parker, *Rev. Sci. Instrum.*, 1997, **68**, 3477-3484.

35. M. L. Weichman, J. A. DeVine, D. S. Levine, J. B. Kim and D. M. Neumark, *P Natl Acad Sci USA*, 2016, **113**, 1698-1705.
36. D. W. Chandler and P. L. Houston, *J. Chem. Phys.*, 1987, **87**, 1445.
37. M. B. Doyle, C. Abeyasera and A. G. Suits, NuACQ, https://chemistry.missouri.edu/people/suits
38. J. R. Gascooke, S. T. Gibson and W. D. Lawrence, *J. Chem. Phys.*, 2017, **147**, 013924.
39. B. Dick, *Phys. Chem. Chem. Phys.*, 2014, **16**, 570.
40. C. Blondel, C. Delsart and F. Goldfarb, *Journal of Physics B-Atomic Molecular and Optical Physics*, 2001, **34**, L281-L288.
41. C. Blondel, W. Chaibi, C. Delsart, C. Drag, F. Goldfarb and S. Kröger, *Eur Phys J D*, 2005, **33**, 335-342.
42. C. Blondel, W. Chaibi, C. Delsart and C. Drag, *J. Phys. B: At. Mol. Opt. Phys.*, 2006, **39**, 1409.
43. J. Cooper and R. N. Zare, *J. Chem. Phys.*, 1968, **48**, 942.
44. E. P. Wigner, *Phys Rev*, 1948, **73**, 1002-1009.
45. M. J. Frisch, G. W. Trucks, H. B. Schlegel, G. E. Scuseria, M. A. Robb, J. R. Cheeseman, G. Scalmani, V. Barone, B. Mennucci, G. A. Petersson, H. Nakatsuji, M. Caricato, X. Li, H. P. Hratchian, A. F. Izmaylov, J. Bloino, G. Zheng, J. L. Sonnenberg, M. Hada, M. Ehara, K. Toyota, R. Fukuda, J. Hasegawa, M. Ishida, T. Nakajima, Y. Honda, O. Kitao, H. Nakai, T. Vreven, J. A. Montgomery, J. E. Peralta, F. Ogliaro, M. Bearpark, J. J. Heyd, E. Brothers, K. N. Kudin, V. N. Staroverov, R. Kobayashi, J. Normand, K. Raghavachari, A. Rendell, J. C. Burant, S. S. Iyengar, J. Tomasi, M. Cossi, N. Rega, J. M. Millam, M. Klene, J. E. Knox, J. B. Cross, V. Bakken, C. Adamo, J. Jaramillo, R. Gomperts, R. E. Stratmann, O. Yazyev, A. J. Austin, R. Cammi, C. Pomelli, J. W. Ochterski, R. L. Martin, K. Morokuma, V. G. Zakrzewski, G. A. Voth, P. Salvador, J. J. Dannenberg, S. Dapprich, A. D. Daniels, Ö. Farkas, J. B. Foresman, J. V. Ortiz, J. Cioslowski and D. J. Fox, Gaussian 09, Revision C.01, http://www.gaussian.com (2009).
46. M. I. M. Sarker, C.-S. Kim and C. H. Choi, *Chem. Phys. Lett.*, 2005, **411**, 297.
47. V. A. Mozhayskiy and A. I. Krylov, ezSpectrum 3.0, http://iopenshell.usc.edu/downloads
48. Y. Liu and C. Ning, *J. Chem. Phys.*, 2015, **143**, 144310.
49. J. A. DeVine, M. L. Weichman, M. C. Babin and D. M. Neumark, *J. Chem. Phys.*, 2017, **147**, 013915.
50. A. Sanov, *Annu. Rev. Phys. Chem.*, 2014, **65**, 341.
51. S. M. O'Malley and D. R. Beck, *J. Phys. B: At. Mol. Opt. Phys.*, 2005, **38**, 2645.
52. C. Duzy and R. S. Berry, *J. Chem. Phys.*, 1976, **64**, 2431.
53. G. Herzberg, *Electronic Spectra of Polyatomic Molecules*, D. Van Nostrand Company, Inc., Princeton, NJ, 1945.
54. J. B. Kim, M. L. Weichman, T. I. Yacovitch, C. Shih and D. M. Neumark, *J. Chem. Phys.*, 2013, **139**, 104301.
55. J. B. Kim, M. L. Weichman and D. M. Neumark, *Phys. Chem. Chem. Phys.*, 2013, **15**, 20973.
56. J. A. DeVine, M. L. Weichman, B. Laws, J. Chang, M. C. Babin, G. Balerdi, C. J. Xie, C. L. Malbon, W. C. Lineberger, D. R. Yarkony, R. W. Field, S. T. Gibson, J. Y. Ma, H. Guo and D. M. Neumark, *Science*, 2017, **358**, 336-339.
57. J. A. DeVine, A. A. Taka, M. C. Babin, M. L. Weichman, H. P. Hratchian and D. M. Neumark, *J. Chem. Phys.*, 2018, **148**, 222810.
58. H. P. Hratchian and H. B. Schlegel, *J. Chem. Phys.*, 2005, **120**, 9918.
59. H. P. Hratchian and H. B. Schlegel, *J. Chem. Theory Comput.*, 2005, **1**, 61.

$$Al_xO_x^- + h\nu \rightarrow Al_xO_x + e^-$$

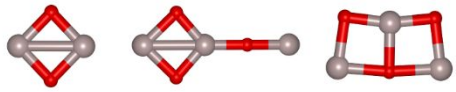

High-resolution photoelectron spectroscopy of cryogenically-cooled aluminum oxide anions show new subtleties in the vibronic structure of $Al_2O_2^{-/0}$ and $Al_3O_3^{-/0}$.